



# Highly efficient Z-Scheme $\text{Ag}_3\text{PO}_4/\text{Ag}/\text{WO}_{3-x}$ photocatalyst for its enhanced photocatalytic performance



Yuyu Bu<sup>a</sup>, Zhuoyuan Chen<sup>a,\*</sup>, Chengjun Sun<sup>b</sup>

<sup>a</sup> Key Laboratory of Marine Environmental Corrosion and Bio-fouling, Institute of Oceanology, Chinese Academy of Sciences, 7 Nanhai Road, Qingdao 266071, China

<sup>b</sup> Marine Ecology Center, The First Institute of Oceanography, State Oceanic Administration, 6 Xianxialing Rd., Qingdao 266061, China

## ARTICLE INFO

### Article history:

Received 26 March 2015

Received in revised form 21 May 2015

Accepted 22 May 2015

Available online 31 May 2015

### Keywords:

Z-scheme

$\text{WO}_{2.72}$

Ag

$\text{Ag}_3\text{PO}_4/\text{Ag}/\text{WO}_{3-x}$

## ABSTRACT

The Z-Scheme  $\text{Ag}_3\text{PO}_4/\text{Ag}/\text{WO}_{3-x}$  photocatalyst was prepared through an *in situ* deposition method. Originally,  $\text{WO}_{2.72}$  with hierarchical sea urchin-like structure was mixed with excessive  $\text{Ag}^+$  ions. The weak reducibility of  $\text{WO}_{2.72}$  was utilized to *in situ* reduce  $\text{Ag}^+$  into Ag, and Ag nanoparticles were deposited on the surface of  $\text{WO}_{2.72}$ . Subsequently, an appropriate amount of  $\text{PO}_4^{3-}$  ions was directly added dropwise to combine with the remaining  $\text{Ag}^+$  ions, as a result, the  $\text{Ag}_3\text{PO}_4$  nanoparticles was, therefore, *in situ* deposited on the surface of  $\text{Ag}/\text{WO}_{3-x}$ , and the Z-Scheme  $\text{Ag}_3\text{PO}_4/\text{Ag}/\text{WO}_{3-x}$  photocatalyst was obtained. The experimental results illustrate that, for the Z-Scheme  $\text{Ag}_3\text{PO}_4/\text{Ag}/\text{WO}_{3-x}$  photocatalyst, Ag nanoparticles serve as carrier-transfer centers, effectively prolong the lifetime of the photoinduced electrons generated by  $\text{Ag}_3\text{PO}_4$  and the photoinduced holes generated by  $\text{WO}_{3-x}$ , and therefore improve the photocatalytic degradation performance. The utilization of the weak reducibility of the transition metal oxides has been explored as an effective strategy to fabricate Z-scheme ‘reduced state transition metal oxide/noble metal/semiconductor’ photocatalysts with enhanced photocatalytic performance.

© 2015 Elsevier B.V. All rights reserved.

## 1. Introduction

Photocatalytic technology is widely regarded as one of the most effective ways to solve the issues of the energy shortage and environmental pollution [1–3]. In the past three decades, researchers have been making unremitting efforts in improving the quantum yields of the photocatalysts. Some new photocatalytic materials with visible light response characteristics and strong photocatalytic capabilities, such as g-C<sub>3</sub>N<sub>4</sub> [4,5],  $\text{Ag}_3\text{PO}_4$  [6,7], P<sub>4</sub> [8,9],  $\text{Ag}/\text{AgX}$  (X = Cl, Br, I) [10–12], were recently developed. By modifying the surface and interface of the photocatalytic materials [13,14], doping [15,16], compositing with other semiconductor materials and adjusting the micro/nano-structures of the photocatalysts [17,18], the photocatalytic performance can be optimized to a great extent. In addition to the above methods, building new photocatalytic systems is also an effective way to improve the photocatalytic quantum yield.

In nature, the green plant is a huge and efficient solar energy conversion system. The photosystems I and II of the plant

photosynthesis harvest photons at 680 and 700 nm, respectively, and oxidize  $\text{H}_2\text{O}$  into  $\text{O}_2$  under sunlight with a quantum yield close to unity. This system went by the name of Z-scheme system [19]. Inspired by the plant photosynthesis, Bard [20] proposed the concept of artificial photosynthesis in 1979. If two visible-light-response photocatalysts with reasonable band energies can be linked via a suitable shuttle redox mediator, visible light will be utilized more efficiently than in the conventional one-step water splitting systems because the energy required for driven each photocatalyst is reduced, similar to the plant photosynthesis. Since the shuttle redox mediator participates in the electron transfer process, complex redox reactions will be occurred, and the energy loss and the electron back transfer during the reactions will be inevitable. Therefore, it has great scientific significance to optimize the process of electron transfer through the shuttle redox mediator. In 2006, Tada and his coworkers [21] prepared CdS-Au-TiO<sub>2</sub> photocatalysts and found that the Au, lied between CdS and TiO<sub>2</sub>, possessed very strong transfer capability of the photogenerated electrons, and it could also induce the annihilation of the photoinduced electrons generated by TiO<sub>2</sub> and the photoinduced holes generated by CdS, thus resulting in leaving the photogenerated electrons with strong reducibility on CdS and the photogenerated holes with high oxidizability on TiO<sub>2</sub>. The mechanism of

\* Corresponding author. Tel.: +86 532 82898731; fax: +86 532 82880498.

E-mail address: [zychen@qdio.ac.cn](mailto:zychen@qdio.ac.cn) (Z. Chen).

the electron transfer in this system is similar to that in shuttle redox mediator aforementioned, thus, it was called as the all-solid-state Z-scheme photocatalyst. Recently, Li et al. [22] successively prepared a TiO<sub>2</sub>-Au-CdS sandwich-type Z-scheme photoanode by depositing Au nanoparticles and CdS quantum dots on the surface of TiO<sub>2</sub> nanorod arrays, and found that its photoelectrochemical performance was strongly enhanced compared to that of TiO<sub>2</sub>-CdS. Their experimental results indicated that the presence of Au could increase the lifetime of the charge carriers, reduced the trap-state Auger rate, suppressed the long-time scale back transfer, partially compensated the negative effects of the surface trap states and thus significantly improved the photoelectrochemical performance of this photoanode. Chen et al. [23] prepared Ag<sub>3</sub>PO<sub>4</sub>/AgI photocatalyst and found that some Ag<sub>3</sub>PO<sub>4</sub> or AgI were gradually reduced to elemental Ag to form Ag<sub>3</sub>PO<sub>4</sub>/AgI@Ag three-phase photocatalyst during the photocatalytic degradation process, resulting in the enhancement of the photocatalytic performance. They attributed the improvement of the photocatalytic properties to the Z-scheme electron transport mechanism. More recently, Ye and his coworkers [24] prepared a series of Ag/AgX/BiOX photocatalysts. They found that the Ag/AgX/BiOX composite with Ag located between AgX and BiOX exhibited much stronger photocatalytic performance than that with Ag existed on the surface of AgX. They suggested that Ag played the role of Z-scheme electron transfer in the Ag/AgX/BiOX composite with Ag located between AgX and BiOX, resulting in the promotion of the photocatalytic performance. Besides the noble metals, a number of transition metals or even nonmetals could also response for the Z-scheme electron transfer. Iwase et al. [25] found that the reduced graphene oxide could play the role of Z-scheme electron transfer after it was embedded between Ru/SrTiO<sub>3</sub>:Rh and BiVO<sub>4</sub>. Wang et al. [26] deposited ZnO nanoparticles onto the surface of Cd particles and prepared ZnO/Cd@CdS composite followed by the formation of CdS coating layer on the surface of Cd by vulcanization. They found that this composite had a superior ability to reduce water into hydrogen in the presence of S<sup>2-</sup> and they suggested that the Cd located between ZnO and CdS played a Z-scheme electron transport role. In addition, CdS was generated directly on the surface of the Cd, which endowed the composite with strong interface bonding and thus dramatically enhanced its photocatalytic performance.

The all-solid-state Z-scheme structure can improve the photocatalytic performance of a photocatalyst, and the transfer capability of the photogenerated electrons is bound to be optimized by further increasing the binding force between the metal and these two semiconductor materials. Therefore, optimizing the binding force on the interfaces between the semiconductor-metal-semiconductor is of great significance. For most types of transition metal oxides, their low valence states or nonstoichiometric numbers often have strong or weak reducing power. Xi et al. [27] prepared sea urchin-like WO<sub>2.72</sub> nanomaterials with reducibility, which was then put into a series of the precursor solutions containing noble metal ions under stirring. The noble metal nanoparticles could be *in situ* deposited on the surface of WO<sub>2.72</sub>. With the increase of the deposited noble metal particles, WO<sub>2.72</sub> was gradually oxidized to WO<sub>3</sub> simultaneously resulting in the formation of very good Schottky junctions between WO<sub>3-x</sub> and the noble metal particles. And this deposition method may have strong application potential in building an excellent all-solid-state Z-Scheme photocatalyst. Recently, Yi et al. [28], for the first time, reported that Ag<sub>3</sub>PO<sub>4</sub> possessed highly efficient photocatalytic water oxidation capability and very good photocatalytic degradation performance of organic dyes under visible light. Afterwards, a large amount of modifying work was developed around Ag<sub>3</sub>PO<sub>4</sub>, such as compositing, controlling of crystal plane and surface modification. However, relatively few studies were focused on building the all-solid-state Z-scheme photocatalyst based on Ag<sub>3</sub>PO<sub>4</sub>. Meanwhile, it also has an important significance

to improve the overall photocatalytic performance by enhancing the binding force of the interfaces between the Ag<sub>3</sub>PO<sub>4</sub>-noble metal-semiconductor. Therefore, in this paper, sea urchin-like WO<sub>2.72</sub> nanomaterials with hierarchical structure and reducibility was firstly prepared, and then this material was transferred into the precursor solution containing excessive Ag<sup>+</sup> ions followed by stirring to form Ag/WO<sub>3-x</sub> composites. Finally, PO<sub>4</sub><sup>3-</sup> ions were directly added drop by drop into the above solution to combine with the remaining Ag<sup>+</sup> ions, and Ag<sub>3</sub>PO<sub>4</sub> particles were directly deposited on the surface of the Ag/WO<sub>3-x</sub> to form the Z-scheme Ag<sub>3</sub>PO<sub>4</sub>/Ag/WO<sub>3-x</sub> photocatalyst. The photocatalytic degradation performance of the prepared Z-scheme Ag<sub>3</sub>PO<sub>4</sub>/Ag/WO<sub>3-x</sub> photocatalyst was studied in this work.

## 2. Experimental

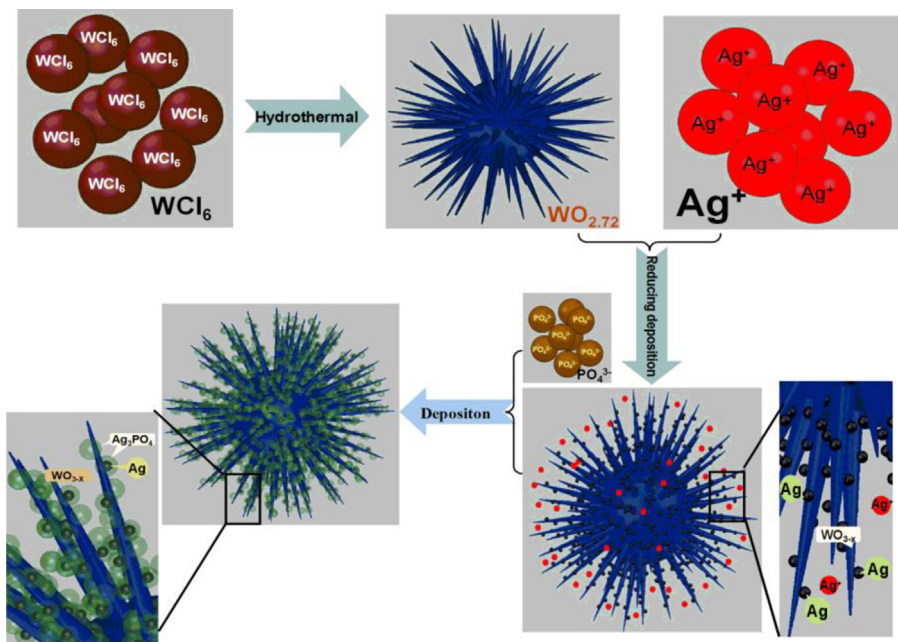
### 2.1. Synthesis of WO<sub>72</sub> and Ag<sub>3</sub>PO<sub>4</sub>/Ag/WO<sub>3-x</sub> composite

Firstly, sea urchin-like WO<sub>2.72</sub> nanomaterials with hierarchical structure were prepared based on the method used by Xi et al. [27]. In a typical synthesis of WO<sub>2.72</sub>, 1.6 g of WCl<sub>6</sub> was added into 80 mL of absolute ethanol, and a clear yellow solution was formed. This solution was then loaded into a 100 mL Teflon-lined autoclave, heated in an oven at 160 °C for 24 h, and then naturally cooled down to room temperature. A blue floccule product was formed, which was then collected, washed with distilled water and ethanol for several times. WO<sub>2.72</sub> was obtained after drying in vacuum for 12 h.

The preparation of the Ag<sub>3</sub>PO<sub>4</sub>/Ag/WO<sub>3-x</sub> composite is as follows. Firstly 0.114 g of WO<sub>2.72</sub> and 0.1 g of polyvinylpyrrolidone were dispersed into 30 mL of deionized water under stirring to form a uniform suspension, and then 20 mL of silver acetate solution with certain concentration was slowly added into this suspension. The suspension was then under stirring for 30 min to make Ag be reduced and be deposited on the surface of WO<sub>2.72</sub>. 25 mL of Na<sub>3</sub>PO<sub>4</sub> solution with certain concentration, which is according to the mole fraction ratio of the added Ag<sup>+</sup> to PO<sub>4</sub><sup>3-</sup> being 1:3, was added drop by drop to the suspension and the suspension was kept stirring for 5 h. The product was centrifuged, rinsed with ethanol and dried at 60 °C. A series of Ag<sub>3</sub>PO<sub>4</sub>/Ag/WO<sub>3-x</sub> composites were obtained with the mass percentage of Ag<sub>3</sub>PO<sub>4</sub> in it being 47 wt%, 64 wt%, 73 wt% and 78 wt%, which were expressed as the 47 wt% Ag<sub>3</sub>PO<sub>4</sub>/Ag/WO<sub>3-x</sub> composite, the 64 wt% Ag<sub>3</sub>PO<sub>4</sub>/Ag/WO<sub>3-x</sub> composite, the 73 wt% Ag<sub>3</sub>PO<sub>4</sub>/Ag/WO<sub>3-x</sub> composite and the 78 wt% Ag<sub>3</sub>PO<sub>4</sub>/Ag/WO<sub>3-x</sub> composite, respectively. The preparation processes of the Z-scheme Ag<sub>3</sub>PO<sub>4</sub>/Ag/WO<sub>3-x</sub> composite were schematically illustrated in Scheme 1.

WO<sub>3</sub> was obtained after sintering WO<sub>2.72</sub> at 500 °C in air for 1 h. The Ag<sub>3</sub>PO<sub>4</sub>/WO<sub>3</sub> composite with 64 wt% Ag<sub>3</sub>PO<sub>4</sub> in it, expressed as the 64 wt% Ag<sub>3</sub>PO<sub>4</sub>/WO<sub>3</sub> composite, was obtained based on the method described above. Pure Ag<sub>3</sub>PO<sub>4</sub> was obtained by adding the Na<sub>3</sub>PO<sub>4</sub> solution, drop by drop, into silver acetate solution and kept stirring for 5 h.

The preparation of the 64 wt% Ag/Ag<sub>3</sub>PO<sub>4</sub>/WO<sub>3</sub> composite is as follows. 0.4 g of the prepared 64 wt% Ag<sub>3</sub>PO<sub>4</sub>/WO<sub>3</sub> composite was added into 50 mL of methanol water solution with 10% volume concentration of methanol. 0.012 g of silver nitrate was then added into this solution. After the added silver nitrate was completely dissolved, the solution was illuminated by a 300 W Xe lamp for 30 min. During the illumination, silver nitrate was reduced and Ag nanoparticles were deposited on the surface of the Ag<sub>3</sub>PO<sub>4</sub>/WO<sub>3</sub> composite. After that, the product was centrifuged, rinsed with ethanol and dried at 60 °C. And the 64 wt% Ag/Ag<sub>3</sub>PO<sub>4</sub>/WO<sub>3</sub> composite was obtained. All reagents used in this study were analytical ones from Aladin Industrial Corporation, China and without any further purification.



**Scheme 1.** Schematic illustration of the preparation processes of the Z-scheme  $\text{Ag}_3\text{PO}_4/\text{Ag}/\text{WO}_{3-x}$  composite.

## 2.2. Characterizations of the prepared photocatalysts

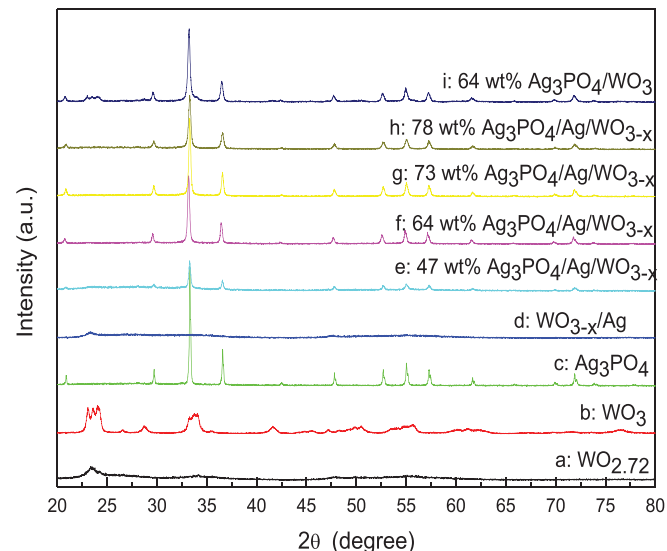
The morphology of the prepared photocatalysts was analyzed using a scanning electron microscope (SEM) (JSM-6700F; JEOL, Tokyo, Japan). The surface information, elemental compositions and bonding information of the synthetic products were analyzed using a field emission high-resolution transmission electron microscope (FE-HRTEM, Tecnai G2 F20, FEI Company, USA), an energy dispersive spectrometer (EDS, FEI Tecnai G20, FEI Company, USA) and X-ray photoelectron spectroscopy (XPS, Axis Ultra, Kratos Analytical Ltd. England). The optical absorption properties were investigated using a UV-vis diffuse reflectance spectrophotometer (U-41000; HITACHI, Tokyo, Japan). The photoluminescence (PL) intensity of the prepared samples was characterized using a fluorescence spectrometer (PL, Fluoro Max-4, HORIBA Jobin Yvon, France). The Brunauer–Emmett–Teller (BET) specific surface area was determined by a multipoint BET method (BET, 3Flex, Micromeritics, USA).

## 2.3. Photocatalytic degradation of Rhodamine B (RhB), methyl orange (MO) and methylene blue (MB)

0.1 g prepared photocatalysts was added to 100 mL dye solution (RhB, MO or MB) with a concentration of  $10 \text{ mg L}^{-1}$  and stirred for 30 min in the dark. The light source was a 300 W Xe arc lamp (PLS-SXE300, Beijing Changtuo Co., Ltd., Beijing, China). A flat circular quartz window with a diameter of 30 mm was on the side of the degradation reactor, and the photo passed through this window and illuminated on the RhB, MO or MB dye solution containing the prepared photocatalysts. A 420-nm cutoff filter was placed in front of the quartz window to remove light with wavelengths less than 420 nm and ultimately generate visible light. The distance between the light source and the dye liquid level is 10 cm. The light intensity is  $200 \text{ mW cm}^{-2}$ . And the temperature was maintained at  $25^\circ\text{C}$  using circulating water.

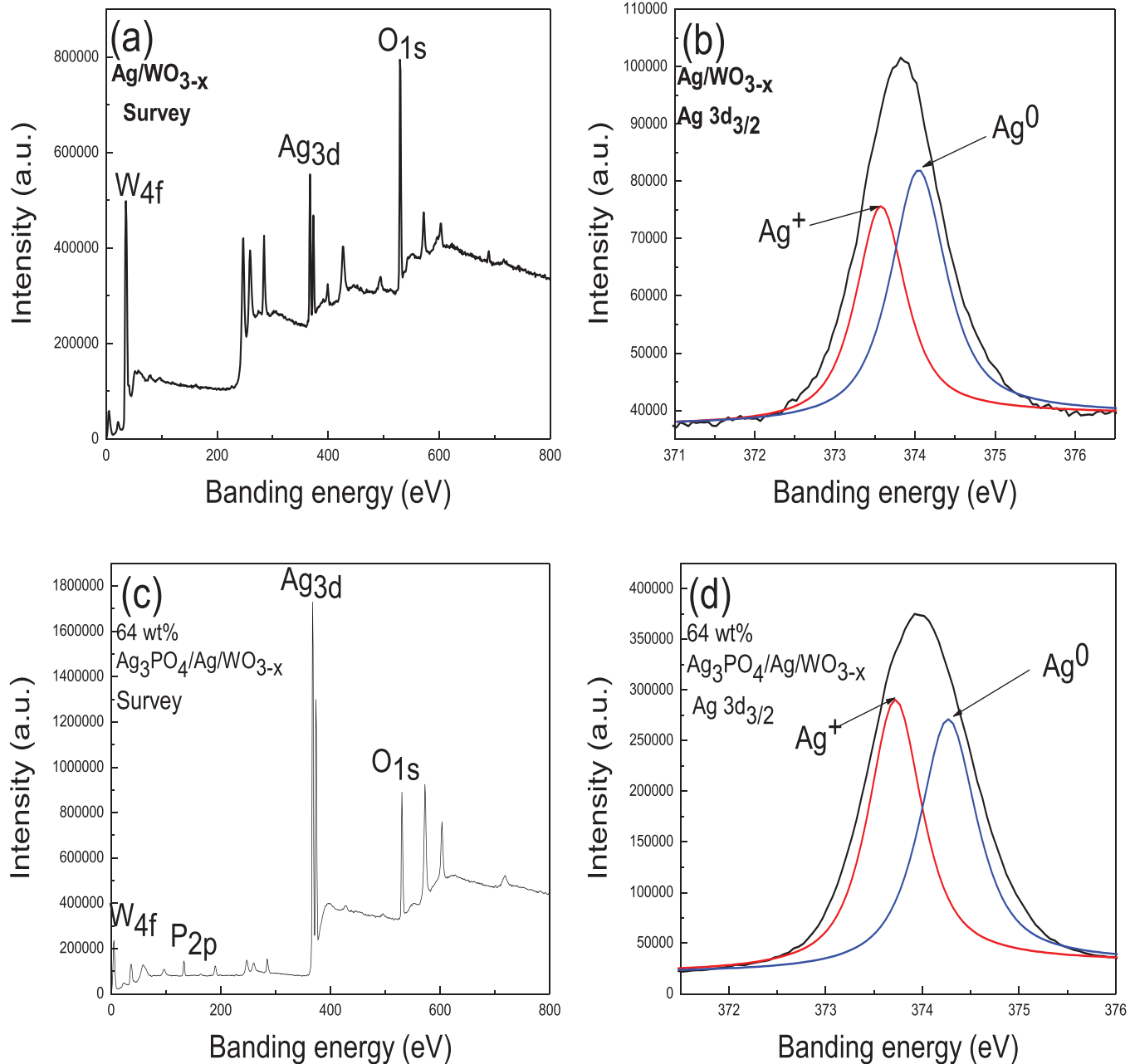
## 3. Results and discussion

Fig. 1 shows the XRD patterns of the prepared samples. Curve 1a shows the XRD pattern of the prepared  $\text{WO}_{2.72}$ , which mainly exists



**Figure 1.** XRD patterns of the prepared (a)  $\text{WO}_{2.72}$ ; (b)  $\text{WO}_3$ ; (c)  $\text{Ag}_3\text{PO}_4$ ; (d)  $\text{Ag}/\text{WO}_{3-x}$ ; (e) 47 wt%  $\text{Ag}_3\text{PO}_4/\text{Ag}/\text{WO}_{3-x}$  composite; (f) 64 wt%  $\text{Ag}_3\text{PO}_4/\text{Ag}/\text{WO}_{3-x}$  composite; (g) 73 wt%  $\text{Ag}_3\text{PO}_4/\text{Ag}/\text{WO}_{3-x}$  composite; (h) 78 wt%  $\text{Ag}_3\text{PO}_4/\text{Ag}/\text{WO}_{3-x}$  composite; (i) 64 wt%  $\text{Ag}_3\text{PO}_4/\text{WO}_3$  composite.

as monoclinic-type configuration. The diffraction peak at  $23.5^\circ$  can be assigned as the  $(0\ 1\ 0)$  lattice plane of  $\text{WO}_{2.72}$  (JCPDS no. 36-101), demonstrating that  $\text{WO}_{2.72}$  was successfully prepared. Curve 1b shows the XRD pattern of the product by sintering  $\text{WO}_{2.72}$  at  $500^\circ\text{C}$  in air. Three diffraction peaks are clearly observed in the range of  $22\text{--}25^\circ$ , which can be assigned as  $(0\ 0\ 2)$ ,  $(0\ 2\ 0)$  and  $(2\ 0\ 0)$  lattice planes of monoclinic  $\text{WO}_3$  (JCPDS 83-0950). Curve 1c shows the XRD pattern of the prepared  $\text{Ag}_3\text{PO}_4$ . The diffraction peaks are the same as those of cubic  $\text{Ag}_3\text{PO}_4$  (JCPDS No. 06-0505), demonstrating that  $\text{Ag}_3\text{PO}_4$  was successfully prepared. Curve 1d shows the XRD pattern of the product by *in situ* depositing Ag on the surface of  $\text{WO}_{2.72}$ . The diffraction peak at  $23.5^\circ$  is observed, however, the intensity of this peak declines by comparing with that of the XRD pattern of  $\text{WO}_{2.72}$  shown in Curve 1a. No diffraction peaks from Ag are observed in Curve 1c. This can be caused by



**Figure 2.** XPS spectra of the prepared Ag/WO<sub>3-x</sub> of (a) the total survey spectrum and (b) the Ag 3d<sub>3/2</sub> XPS core level spectrum; and the prepared 64 wt% Ag<sub>3</sub>PO<sub>4</sub>/Ag/WO<sub>3-x</sub> composite of (c) the total survey spectrum and (d) the Ag 3d<sub>3/2</sub> XPS core level spectrum.

the lower proportion of the deposited Ag (<1.5%), resulting in the absence of the XRD diffraction peaks of Ag. Curves 1e, 1f, 1g and 1h show the XRD patterns of the Ag<sub>3</sub>PO<sub>4</sub>/Ag/WO<sub>3-x</sub> composites containing with 47 wt% (Curve 1e), 64 wt% (Curve 1f), 73 wt% (Curve 1g) and 78 wt% (Curve 1h) Ag<sub>3</sub>PO<sub>4</sub>, respectively. Comparing with these patterns, the diffraction peaks of cubic Ag<sub>3</sub>PO<sub>4</sub> appear when the mass ratio of Ag<sub>3</sub>PO<sub>4</sub> in this composite reaches 47 wt%, and the intensities of those peaks are gradually enhanced with the increase of the mass ratio of Ag<sub>3</sub>PO<sub>4</sub> in this composite. The diffraction peak at 23.5° disappears, which may be due to the coverage of Ag<sub>3</sub>PO<sub>4</sub> after compositing WO<sub>2.72</sub> with Ag<sub>3</sub>PO<sub>4</sub>. Curve 1i shows the XRD pattern of the 64 wt% Ag<sub>3</sub>PO<sub>4</sub>/WO<sub>3</sub> composite. Except for the characteristic diffraction peaks of cubic Ag<sub>3</sub>PO<sub>4</sub>, three diffraction peaks of WO<sub>3</sub> in the range of 22–25° can still be observed, indicating that the Ag<sub>3</sub>PO<sub>4</sub>/WO<sub>3</sub> composite was successfully prepared.

The elemental compositions of the prepared samples and the valence states of Ag were further analyzed using XPS, and the relevant results are shown in Fig. 2. Fig. 2a shows the XPS survey spectrum of the Ag/WO<sub>3-x</sub> composite, and the results indicate that the composite is mainly composed of elements W, O and Ag. Fig. 2b shows the Ag 3d<sub>3/2</sub> XPS core level spectrum of the Ag/WO<sub>3-x</sub> composite. Two binding energy peaks at 373.5 eV and 374.2 eV are observed in Fig. 2b, which can be attributed to Ag<sup>+</sup> and Ag, respectively [23,29]. The results indicate that some of Ag<sup>+</sup> were reduced into Ag on the surface of WO<sub>2.72</sub> and partial Ag<sup>+</sup> ions were adsorbed on the surface of WO<sub>2.72</sub> in the mean time after stirring the mixture of WO<sub>2.72</sub> and Ag<sup>+</sup> for 30 min. Meanwhile, Fig. S1 gives the W<sub>4f</sub> XPS core level spectrum of the prepared WO<sub>2.72</sub> and Ag/WO<sub>3-x</sub> composite, and the W<sub>4f</sub> peak negatively shifts after the formation of reduced Ag on the surface of WO<sub>2.7</sub>, which can be explained as the gradual increase of the valence of element W in WO<sub>2.72</sub> dur-

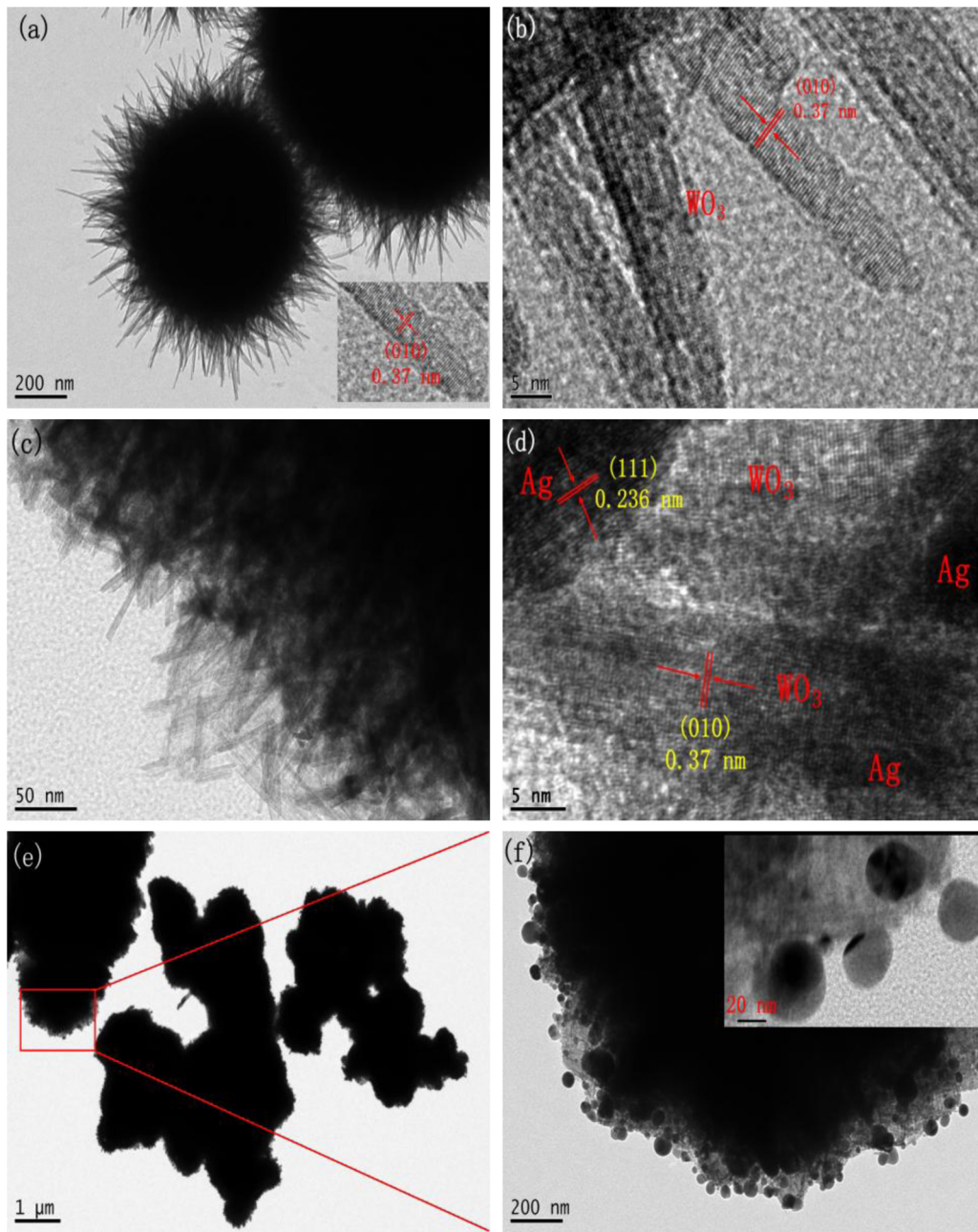


**Figure 3.** TEM images of the prepared (a) low-resolution  $\text{WO}_{2.72}$ ; (b) high-resolution  $\text{WO}_{2.72}$ ; (c) low-resolution  $\text{Ag}/\text{WO}_{3-x}$ ; (d) high-resolution  $\text{Ag}/\text{WO}_{3-x}$ ; (e) low-resolution 64 wt%  $\text{Ag}_3\text{PO}_4/\text{Ag}/\text{WO}_{3-x}$ ; and (f) high-resolution 64 wt%  $\text{Ag}_3\text{PO}_4/\text{Ag}/\text{WO}_{3-x}$ .

ing the formation process of Ag on the surface of  $\text{WO}_{2.72}$ , Fig. 2c shows the XPS survey spectrum of the 64 wt%  $\text{Ag}_3\text{PO}_4/\text{Ag}/\text{WO}_{3-x}$  composite, and the elements of W, O, P and Ag are observed from this spectrum. Fig. 2d shows the  $\text{Ag}3\text{d}_{3/2}$  XPS core level spectrum of 64 wt%  $\text{Ag}_3\text{PO}_4/\text{Ag}/\text{WO}_{3-x}$  composite. Similar to Fig. 2b, two binding energy peaks at 373.5 eV and 374.2 eV are observed by curve fitting. And the intensities of these two peaks shown in Fig. 2d are significantly increased by comparing with those shown in Fig. 2b.

The morphologies of the prepared samples are characterized by TEM, and the relevant results are shown in Fig. 3. Fig. 3a shows the TEM morphology of  $\text{WO}_{2.72}$ . Obviously, sea urchin-like hierarchical structured  $\text{WO}_{2.72}$  was successfully prepared with the overall diameter of approximately 1  $\mu\text{m}$  and the solid core diameter of approximately 800 nm. The length of the branches surrounding the solid core of the sea urchin-like hierarchical structured  $\text{WO}_{2.72}$  is approximately 200 nm. And the branches of  $\text{WO}_{2.72}$  with 0.37 nm

of (010) crystal plane can be clearly observed under higher magnification, as shown in Fig. 3b. Fig. S2a shows the SEM image of  $\text{WO}_{2.72}$ , from which the sea urchin-like hierarchical structured  $\text{WO}_{2.72}$  with the diameter of approximately 1  $\mu\text{m}$  was observed. Fig. 3c shows the TEM morphology of  $\text{Ag}/\text{WO}_{3-x}$ . In contrast to Fig. 3a, the length of the branches is decreased while the diameter of the solid core is increased. Fine particles are observed, which could probably be due to the formation of Ag nanoparticles on the surface of  $\text{WO}_{2.72}$ . Fig. 3d shows morphology the  $\text{Ag}/\text{WO}_{3-x}$  under the high-resolution TEM, from which the Ag nanoparticles with 0.236 nm of (111) crystal plane can be found on the surface of  $\text{WO}_{3-x}$ . Fig. 3e shows the microscopic morphology of the 64 wt%  $\text{Ag}_3\text{PO}_4/\text{Ag}/\text{WO}_{3-x}$  composite under low-resolution TEM, and the results indicate that the sea urchin-like  $\text{WO}_{2.72}$  with hierarchical structure is completely disappeared. The gaps between the branches were filled with other particulate materials, resulting in

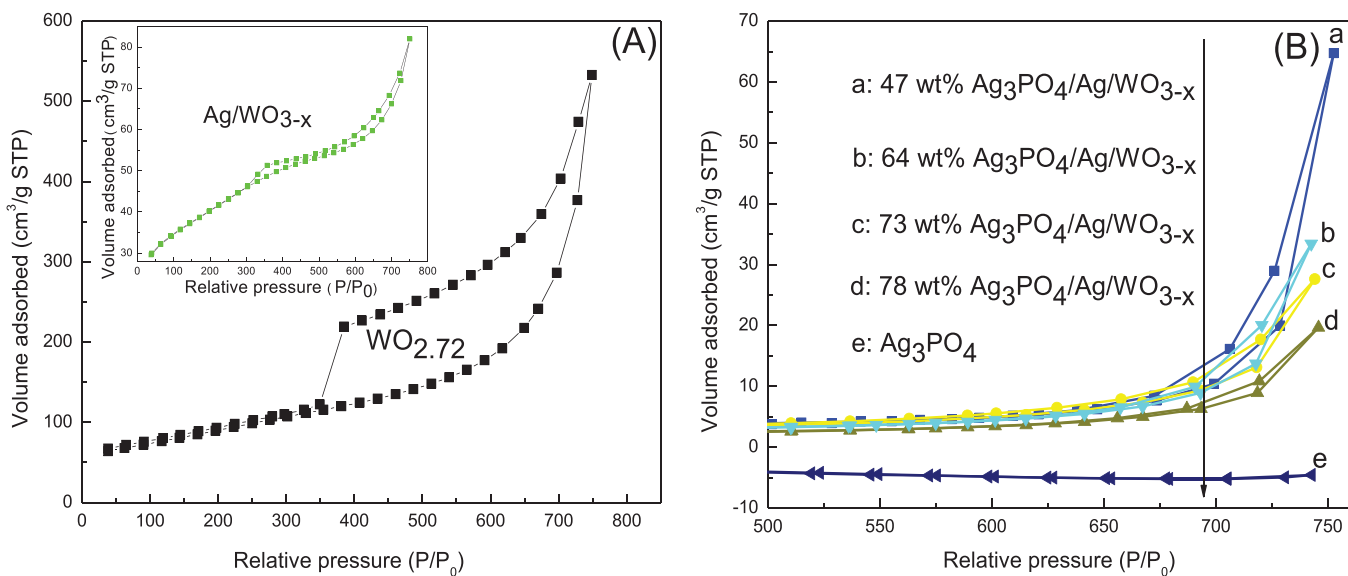


**Figure 4.** The nitrogen adsorption/desorption isotherms of the prepared (A) WO<sub>2.72</sub> and Ag/WO<sub>3-x</sub>; and (B) the prepared Ag<sub>3</sub>PO<sub>4</sub> and Ag<sub>3</sub>PO<sub>4</sub>/Ag/WO<sub>3-x</sub> composites with different Ag<sub>3</sub>PO<sub>4</sub> mass ratios.

the formation of solid spherical particles with very thin outer layers and very thick inner cores. The solid spherical particle in Fig. 3e was further enlarged and the relevant results are shown in Fig. 3f. A large amount of particles with the diameter of approximately 40 nm are distributed on the solid sphere, which are the Ag<sub>3</sub>PO<sub>4</sub> particles deposited on the surface of Ag/WO<sub>3-x</sub>. Fig. S2b shows the SEM image of the 64 wt% Ag<sub>3</sub>PO<sub>4</sub>/Ag/WO<sub>3-x</sub> composite. The sea urchin-like W<sub>2.72</sub> is filled with a large amount of particulates and a solid sphere is formed, which is similar to that observed in Fig. 3e. Fig. S3 shows the EDS results of the 64 wt% Ag<sub>3</sub>PO<sub>4</sub>/Ag/WO<sub>3-x</sub> composite. W, Ag, P and O elements are observed, which are consistent with the elemental compositions of the Ag<sub>3</sub>PO<sub>4</sub>/Ag/WO<sub>3-x</sub> composite. The abovementioned results indicate that the three-phase Ag<sub>3</sub>PO<sub>4</sub>/Ag/WO<sub>3-x</sub> composite was prepared via the *in situ* reduction of Ag<sup>+</sup> and the subsequent simple deposition process.

Fig. 4 shows the nitrogen adsorption/desorption isotherms of WO<sub>2.72</sub>, Ag/WO<sub>3-x</sub>, Ag<sub>3</sub>PO<sub>4</sub> and Ag<sub>3</sub>PO<sub>4</sub>/Ag/WO<sub>3-x</sub> composites with different Ag<sub>3</sub>PO<sub>4</sub> mass ratios, and Table 1 shows the BET specific surface areas obtained based on the results shown in Fig. 4. Fig. 4A shows the nitrogen adsorption/desorption isotherms of WO<sub>2.72</sub> and Ag/WO<sub>3-x</sub>. The isotherms of WO<sub>2.72</sub> and Ag/WO<sub>3-x</sub> are of type IV classification and both of them have typical hysteresis loops of mesoporous materials. As shown in Table 1, the surface area of the hierarchical sea urchin-like WO<sub>2.72</sub> reaches 293.95 m<sup>2</sup> g<sup>-1</sup>. Such a large specific surface area can provide a large number of loading sites for depositing other materials. After loading Ag on the surface of WO<sub>2.72</sub>, the corresponding specific surface area decreases to 143.82 m<sup>2</sup> g<sup>-1</sup>. The decrease of the specific surface area of Ag/WO<sub>3-x</sub> is mainly resulted from the loading of Ag and Ag<sup>+</sup> on the surface of WO<sub>2.72</sub>. Fig. 4B shows the nitrogen adsorption/desorption isotherms of Ag<sub>3</sub>PO<sub>4</sub> and the Ag<sub>3</sub>PO<sub>4</sub>/Ag/WO<sub>3-x</sub> composites with different Ag<sub>3</sub>PO<sub>4</sub> mass ratios. With the increase of the mass ratio of Ag<sub>3</sub>PO<sub>4</sub>, type IV classification of the isotherms gradually disappears and the corresponding specific surface areas, as shown in Table 1, dramatically decrease. These results indicate

that Ag<sub>3</sub>PO<sub>4</sub> may be gradually filled in the mesoporous structure of WO<sub>2.72</sub>, resulting in the decrease of the specific surface areas.

UV/vis diffuse reflectance spectrum was measured to characterize the optical bandgap and absorption capability of the prepared photocatalysts. Fig. 5A shows the UV/vis diffuse reflectance spectra of the prepared WO<sub>2.72</sub>, Ag/WO<sub>3-x</sub> and WO<sub>3</sub>. The absorption band edge of WO<sub>2.72</sub> locates at approximately 450 nm. As shown in Fig. 5A, the absorption values strongly rise at >450 nm, which is due to the presence of a large amount of oxygen defects in WO<sub>2.72</sub>. The oxygen defects can introduce new doping levels under the conduction band and the band gaps between these doping levels and the conduction band of WO<sub>2.72</sub> are very small, resulting in the light absorption in the entire visible region and even in the infrared region. The absorption band edge of Ag/WO<sub>3-x</sub> is consistent with that of WO<sub>2.7</sub>. However, the rise of the absorption value does not appear when the wavelength of light is larger than 450 nm. This can be explained as follows. WO<sub>2.72</sub> provides the electrons to reduce Ag<sup>+</sup> and WO<sub>2.72</sub> itself is oxidized at the meantime, as a result, the number of oxygen defects declines and this upward trend of the light absorption is suppressed. The absorption threshold of WO<sub>3</sub> has a small red shift compared with that of WO<sub>2.72</sub>, while the absorption values at the wavelength larger than 450 nm are maintained at lower levels compared with those of WO<sub>2.72</sub> and Ag/WO<sub>3-x</sub>, indicating that the amount of oxygen defects in WO<sub>2.72</sub> has been significantly decreased after the high-temperature treatment in air. Fig. 5B shows the UV/vis diffuse reflectance spectra of Ag<sub>3</sub>PO<sub>4</sub>, the 64 wt% Ag<sub>3</sub>PO<sub>4</sub>/WO<sub>3</sub> composite and the Ag<sub>3</sub>PO<sub>4</sub>/Ag/WO<sub>3-x</sub> composites with different Ag<sub>3</sub>PO<sub>4</sub> mass ratios. The absorption peak at around of 450–500 nm is contributed from Ag<sub>3</sub>PO<sub>4</sub> and the absorption peak at around of 250–300 nm is the joint contribution from WO<sub>3-x</sub> and Ag<sub>3</sub>PO<sub>4</sub>. When the excitation wavelength is larger than 500 nm, the absorption of Ag<sub>3</sub>PO<sub>4</sub>/WO<sub>3</sub> is of absence and the absorption of Ag<sub>3</sub>PO<sub>4</sub> decreases rapidly with the increase of the wavelength. The Ag<sub>3</sub>PO<sub>4</sub>/Ag/WO<sub>3-x</sub> composites with different Ag<sub>3</sub>PO<sub>4</sub> mass ratios can still absorb light in the

**Table 1**

BET surface area of the prepared WO<sub>2.72</sub>, Ag/WO<sub>3-x</sub>, and Ag<sub>3</sub>PO<sub>4</sub>/Ag/WO<sub>3-x</sub> composites with different Ag<sub>3</sub>PO<sub>4</sub> mass ratios.

Sample	WO <sub>2.72</sub>	Ag/WO <sub>3-x</sub>	47 wt% Ag <sub>3</sub> PO <sub>4</sub> /Ag/WO <sub>3-x</sub>	64 wt% Ag <sub>3</sub> PO <sub>4</sub> /Ag/WO <sub>3-x</sub>	73 wt% Ag <sub>3</sub> PO <sub>4</sub> /Ag/WO <sub>3-x</sub>	78 wt% Ag <sub>3</sub> PO <sub>4</sub> /Ag/WO <sub>3-x</sub>	Ag <sub>3</sub> PO <sub>4</sub>
Surface area (m <sup>2</sup> g <sup>-1</sup> )	93.95	143.82	10.83	9.33	9.16	7.38	3.88

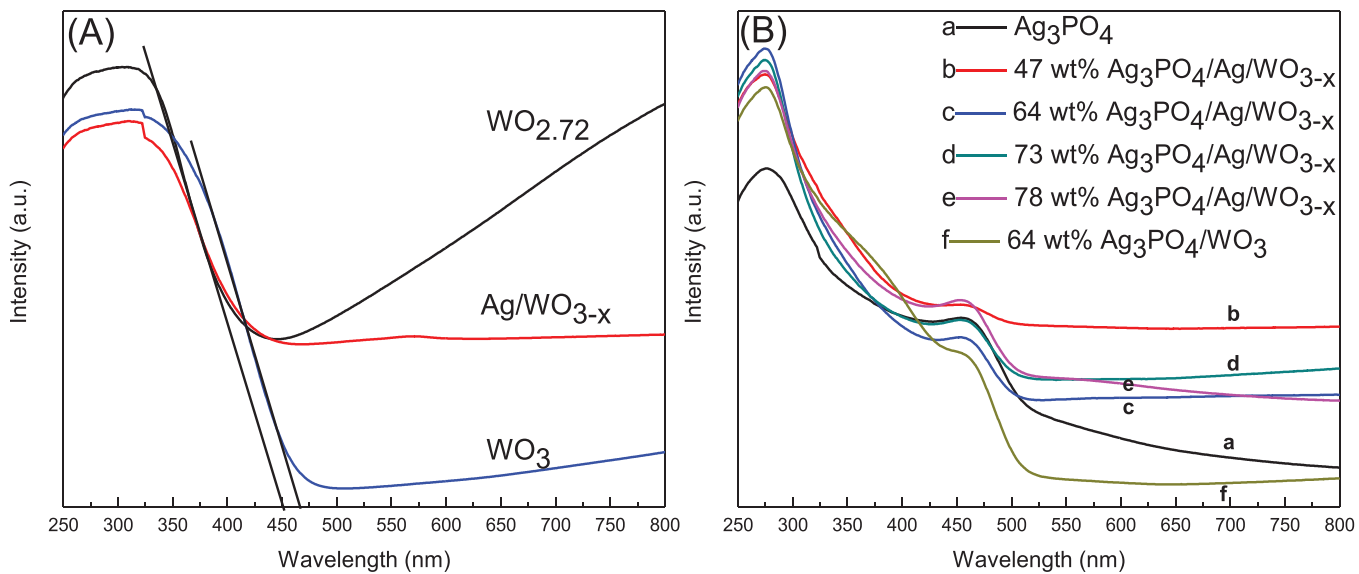


**Figure 5.** UV/Vis diffuse reflection spectra of (A)  $\text{WO}_{2.72}$ ,  $\text{Ag}/\text{WO}_{3-\text{x}}$  and  $\text{WO}_3$ ; and (B)  $\text{Ag}_3\text{PO}_4$  and the  $\text{Ag}_3\text{PO}_4/\text{Ag}/\text{WO}_{3-\text{x}}$  composites with different  $\text{Ag}_3\text{PO}_4$  mass ratios.

excitation wavelength  $>500$  nm. The  $\text{Ag}_3\text{PO}_4/\text{Ag}/\text{WO}_{3-\text{x}}$  composite with 47 wt%  $\text{Ag}_3\text{PO}_4$  has the strongest light absorption, as shown in Fig. 5B.

Photocatalytic performance of the prepared photocatalysts was characterized by testing the capability of the photocatalytic decolorization of the dye, and the relevant results are shown in Fig. 6. Fig. 6A shows the RhB degradation curves of the prepared photocatalysts under visible light. Curve 6Aa is the RhB degradation curve of  $\text{WO}_3$ , and about 20% of the RhB dye is degraded by  $\text{WO}_3$  after 12 min of illumination. Curve 6Ab is the RhB degradation curve of  $\text{WO}_{2.72}$ , and about 40% of the RhB dye is absorbed by  $\text{WO}_{2.72}$  after reaching the adsorption equilibrium by stirring for 30 min in the dark. This could be caused by the large specific surface area of  $\text{WO}_{2.72}$ . Afterwards, the RhB dye concentration fell by only 10% after 12 min of illumination. The above results indicate that both  $\text{WO}_3$  and  $\text{WO}_{2.72}$  show a weak RhB degradation capability. Curve 6Ag is the RhB degradation curve of  $\text{Ag}_3\text{PO}_4$ , and it shows that  $\text{Ag}_3\text{PO}_4$  can realize the total decolorization of RhB within 12 min. Curves 6Ac–f are the RhB degradation curves of the prepared Z-scheme 47 wt% (Curves 6Ac), 64 wt% (Curves 6Ad), 73 wt% (Curves 6Ae) and 78 wt% (Curves 6Af)  $\text{Ag}_3\text{PO}_4/\text{Ag}/\text{WO}_{3-\text{x}}$  photocatalysts. The photocatalytic RhB degradation efficiency increases with the increase of the mass ratio of  $\text{Ag}_3\text{PO}_4$  in the  $\text{Ag}_3\text{PO}_4/\text{Ag}/\text{WO}_{3-\text{x}}$  composites. When the mass ratio of  $\text{Ag}_3\text{PO}_4$  in the  $\text{Ag}_3\text{PO}_4/\text{Ag}/\text{WO}_{3-\text{x}}$  composite is 64 wt%, the photocatalytic degradation efficiency reached the maximum value (i.e., the optimal photocatalytic degradation efficiency). All RhB were degraded after only 3 min of illumination by visible light, and the photocatalytic RhB degradation performance increased four times by comparing with that of pure  $\text{Ag}_3\text{PO}_4$ . With the further increase of the mass ratio of  $\text{Ag}_3\text{PO}_4$ , the photocatalytic degradation efficiency decreases.

To highlight the advantages of Ag as an intermediate to transfer electrons, the photocatalytic RhB degradation performance of 64 wt%  $\text{Ag}_3\text{PO}_4/\text{WO}_3$  composite was tested for comparison, and the results are shown in Curve 6Ah. It costs about 11 min to degrade all of the RhB by this composite. Thus, the photocatalytic RhB degradation performance of the  $\text{Ag}_3\text{PO}_4/\text{WO}_3$  photocatalysts can be significantly improved by locating Ag between  $\text{Ag}_3\text{PO}_4$  and  $\text{WO}_{3-\text{x}}$ . In this work, the 64 wt%  $\text{Ag}/\text{Ag}_3\text{PO}_4/\text{WO}_3$  composite was prepared by *in situ* depositing Ag nanoparticles on the surface of the 64 wt%  $\text{Ag}_3\text{PO}_4/\text{WO}_3$  composite using a photo-assisted reduction method. The photocatalytic RhB degradation performance of the 64 wt%  $\text{Ag}/\text{Ag}_3\text{PO}_4/\text{WO}_3$  composite was also measured and the

results are shown in Curve 6Ai. It costs 10 min for the 64 wt%  $\text{Ag}/\text{Ag}_3\text{PO}_4/\text{WO}_3$  composite to completely degrade all of the RhB. As shown in Fig. 6A, the RhB degradation performance of the 64 wt%  $\text{Ag}/\text{Ag}_3\text{PO}_4/\text{WO}_3$  composite is much poorer than that of the 64 wt%  $\text{Ag}_3\text{PO}_4/\text{Ag}/\text{WO}_{3-\text{x}}$  composite, indicating that the existence of Ag nanoparticles between the  $\text{Ag}_3\text{PO}_4$  and  $\text{WO}_3$  phases leads to a much better photocatalytic degradation performance. This indicates, to a certain extent, that Ag has an intermediate electron transfer function caused by the Z-scheme effect when Ag nanoparticles are located between the  $\text{Ag}_3\text{PO}_4$  and  $\text{WO}_3$ .

The photocatalytic RhB, MB and MO dye degradation performance of the 64 wt%  $\text{Ag}_3\text{PO}_4/\text{Ag}/\text{WO}_{3-\text{x}}$  composite under visible light was further examined and compared, and the relevant results are shown in Fig. 6B. The experimental results indicate that this photocatalyst can degrade all of the RhB in 3 min and all of the MB in 2 min under visible light. However, it costs 20 min for this composite to degrade all of the MO under visible light. This is caused by the different photocatalytic degradation mechanism of MO. In the photocatalytic degradation process of MO,  $\text{O}_2^\bullet$  plays the primary role, while hole and  $\text{HO}^\bullet$  play a minor role.[30] The  $\text{O}_2^\bullet$  is mainly originated from the capture of the photogenerated electrons by the dissolved oxygen. However, the potentials of the photoinduced electrons generated by both  $\text{Ag}_3\text{PO}_4$  and  $\text{WO}_{3-\text{x}}$  are very positive because their conduction band potentials are more positive. Therefore, the photogenerated electrons are difficult to combine with the dissolved  $\text{O}_2$  to form  $\text{O}_2^\bullet$ .

Because RhB, MB and MO have a certain extent of dye sensitization effect on photocatalyst, the self-degradation of the dye can occur quickly under visible light. In order to avoid this process, the colorless phenol is selected as the target degradation substance. The photocatalytic degradation tests of the 64 wt%  $\text{Ag}_3\text{PO}_4/\text{Ag}/\text{WO}_{3-\text{x}}$  composite are performed in the colorless phenol by recording the data of UV/vis absorption spectra of the phenol solution after different time of visible light illumination, and the results are shown in Fig. 7. Curve 7a is the UV/vis absorption spectrum of the phenol in the dark, and the absorption peak at 269.5 nm corresponds to the characteristic absorption of phenol. After 20 min of visible light irradiation (Curve 7b), the intensity of the absorption peak at 269.5 nm is significantly decreased, while, the adsorption peak at 243.5 nm, which is the characteristic peak of p-benzoquinone, is appeared, indicating that the some of the phenol are transformed into p-benzoquinone under the photocatalysis of the 64 wt%  $\text{Ag}_3\text{PO}_4/\text{Ag}/\text{WO}_{3-\text{x}}$  composite. With the

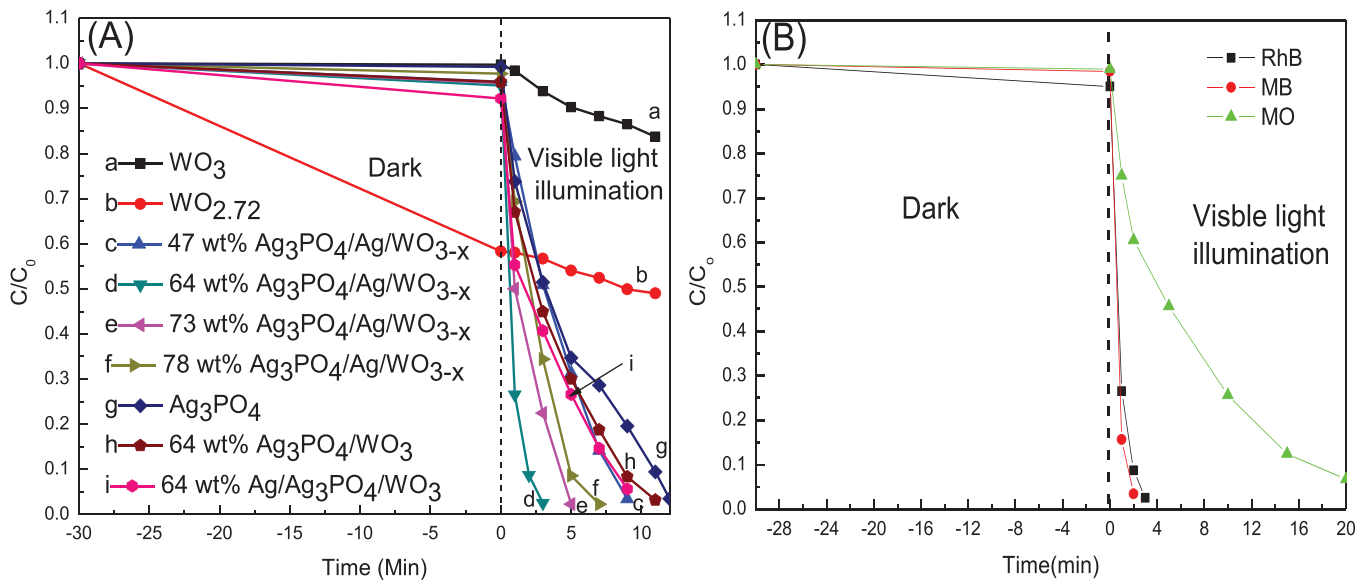


**Figure 6.** (A) Rhodamine B dye degradation curves of the prepared photocatalysts of  $\text{WO}_3$ ,  $\text{WO}_{2.72}$ ,  $\text{Ag}_3\text{PO}_4$ , the 64 wt%  $\text{Ag}_3\text{PO}_4/\text{WO}_3$  composite, the 64 wt%  $\text{Ag}/\text{Ag}_3\text{PO}_4/\text{WO}_3$  composite and the  $\text{Ag}_3\text{PO}_4/\text{Ag}/\text{WO}_{3-x}$  composites with different mass ratios of  $\text{Ag}_3\text{PO}_4$  under visible light; (B) RhB, MB and MO dye degradation curves of the prepared 64 wt%  $\text{Ag}_3\text{PO}_4/\text{Ag}/\text{WO}_{3-x}$  under visible light.

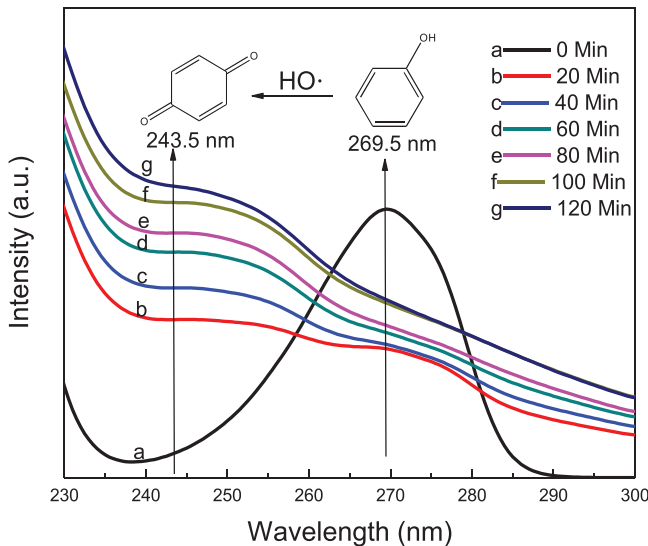


**Figure 7.** UV/vis absorption spectra of the photocatalytic degraded phenol by the 64 wt%  $\text{Ag}_3\text{PO}_4/\text{Ag}/\text{WO}_{3-x}$  composite under different time of visible light illumination.

further increase of the illumination duration, the absorption peak of phenol at 269.5 nm fades away and turns into a slash, and the absorption peak of p-benzoquinone at 243.5 nm shows a rising trend. The results indicate that the 64 wt%  $\text{Ag}_3\text{PO}_4/\text{Ag}/\text{WO}_{3-x}$  composite can selectively oxidize phenol into p-benzoquinone under visible light [31,32]. During the photocatalytic process, the free radicals, including hole,  $\text{HO}^\bullet$  and  $\text{O}_2^\bullet$ , take the primary photocatalytic effect. P-Benzoquinone is particularly sensitive to  $\text{O}_2^\bullet$  and it is not sensitive to hole and  $\text{HO}^\bullet$ , thus, it can serve as the characteristic capturing agent of  $\text{O}_2^\bullet$ . For the 64 wt%  $\text{Ag}_3\text{PO}_4/\text{Ag}/\text{WO}_{3-x}$  composite, both  $\text{WO}_{3-x}$  and  $\text{Ag}_3\text{PO}_4$ , which play the role of the photoelectric conversion, have very positive valence bands. Thus, the photoinduced holes generated by them or the formed  $\text{HO}^\bullet$  radicals have very strong oxidation capability, which can achieve rapid oxidative degradation of some dyes. However, both of them have very positive conduction bands, resulting in the generation of the photo-

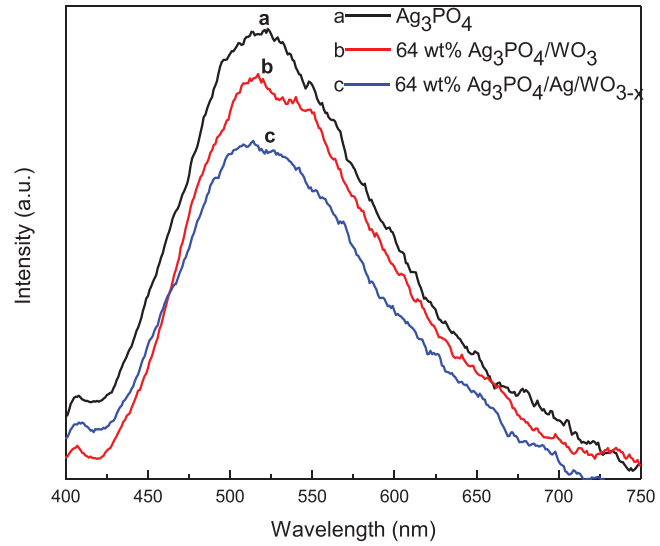


**Figure 8.** The photoluminescence spectra of the prepared  $\text{Ag}_3\text{PO}_4$ , 64 wt%  $\text{Ag}_3\text{PO}_4/\text{WO}_3$  and 64 wt%  $\text{Ag}_3\text{PO}_4/\text{Ag}/\text{WO}_{3-x}$  composite.

toinduced electrons with very weak reducibility. Therefore, it is difficult for the photoinduced electrons generated by them to capture the dissolved oxygen to form  $\text{O}_2^\bullet$ , and p-benzoquinone cannot continue the further conversion process. Consequently, the 64 wt%  $\text{Ag}_3\text{PO}_4/\text{Ag}/\text{WO}_{3-x}$  composite can only selectively convert phenol into p-benzoquinone under visible light.

The Ag loaded between  $\text{WO}_{3-x}$  and  $\text{Ag}_3\text{PO}_4$  can act as the intermediate for transferring electrons and induce the recombination of the photoinduced holes generated by  $\text{Ag}_3\text{PO}_4$  and the photoinduced electrons generated by  $\text{WO}_{3-x}$ , resulting in the prolongation of the lifetime of the photogenerated electrons on the conduction band of  $\text{Ag}_3\text{PO}_4$  and the photogenerated holes in the valence band of  $\text{WO}_{3-x}$ . The PL spectra can be used to study the lifetime of the photogenerated electrons. If the lifetime of the photoinduced electrons generated by  $\text{Ag}_3\text{PO}_4$  is prolonged, the intensities of the luminous peaks in the PL spectra will be very weak. Fig. 8 shows the PL spectra of  $\text{Ag}_3\text{PO}_4$  (Curve a), 64 wt%  $\text{Ag}_3\text{PO}_4/\text{WO}_3$  (Curve

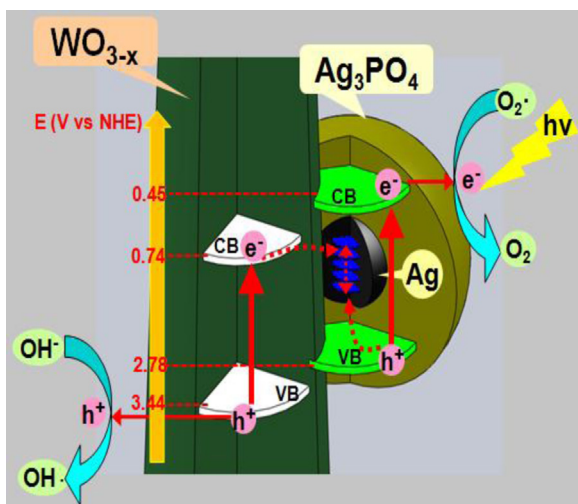


**Figure 9.** Proposed mechanism for the Z-scheme charge-carrier transfer process in the  $\text{Ag}_3\text{PO}_4/\text{Ag}/\text{WO}_{3-x}$  composite.

8b) and 64 wt%  $\text{Ag}_3\text{PO}_4/\text{Ag}/\text{WO}_{3-x}$  (Curve 8c). The luminous peak of these three photocatalysts is observed at around of 520 nm. The intensity of the luminous peak of 64 wt%  $\text{Ag}_3\text{PO}_4/\text{WO}_3$  is weaker than that of  $\text{Ag}_3\text{PO}_4$ , indicating that the heterojunction electric field formed between  $\text{WO}_3$  and  $\text{Ag}_3\text{PO}_4$  inhibits the secondary recombination of the photoinduced electrons and holes to some extent. The intensity of the luminous peak of the 64 wt%  $\text{Ag}_3\text{PO}_4/\text{Ag}/\text{WO}_{3-x}$  composite shows a further decline by comparing with that of the 64 wt%  $\text{Ag}_3\text{PO}_4/\text{WO}_3$  composite, demonstrating that the existence of Ag in this composite can further effectively increase the lifetime of the photoinduced electrons generated by  $\text{Ag}_3\text{PO}_4$  and the photoinduced holes generated by  $\text{WO}_{3-x}$ , and thus improving its photocatalytic degradation performance [33,34].

Fig. 9 schematically shows the proposed promotion mechanism of the photocatalytic degradation performance of the Z-scheme  $\text{Ag}_3\text{PO}_4/\text{Ag}/\text{WO}_{3-x}$  composite. The locations of the band potentials of  $\text{WO}_{3-x}$  and  $\text{Ag}_3\text{PO}_4$  are also schematically illustrated in this figure [23,27,35]. The Ag particles deposited on the surface of  $\text{WO}_{3-x}$  can form good schottky junctions by contacting Ag with  $\text{WO}_{3-x}$ , and the photoinduced electrons generated by  $\text{WO}_{3-x}$  under incident visible light illumination can be quickly transferred to Ag. In the meanwhile, the  $\text{Ag}_3\text{PO}_4$  grown on the Ag surface can contact very well with Ag, and the photoinduced holes generated by  $\text{Ag}_3\text{PO}_4$  under the incident visible light illumination can move quickly to Ag, thus inducing the annihilation of the photogenerated electrons with weak reducibility and photogenerated holes with weak oxidizability. Therefore, the photoinduced electrons with strong reducibility are left on the conduction band of  $\text{Ag}_3\text{PO}_4$ , and the photoinduced holes with strong oxidizability are left on the valence band of  $\text{WO}_{3-x}$ . These photogenerated electrons and holes will then participate in the redox reactions of the organic dyes, resulting in the promotion of the photocatalytic degradation performance of this photocatalyst.

#### 4. Conclusions

Using the reducibility of the hierarchical sea-urchin structured  $\text{WO}_{2.72}$ , the Z-scheme  $\text{Ag}_3\text{PO}_4/\text{Ag}/\text{WO}_{3-x}$  photocatalyst was prepared. The Ag located between the  $\text{WO}_{3-x}$  and  $\text{Ag}_3\text{PO}_4$  plays the role of the Z-scheme charge-carrier transfer during the photocatalytic degradation process, which effectively prolongs the lifetime of the photoinduced electrons generated by  $\text{Ag}_3\text{PO}_4$  and the photoinduced holes generated by  $\text{WO}_{3-x}$ . The  $\text{Ag}_3\text{PO}_4/\text{Ag}/\text{WO}_{3-x}$  composite with 64 wt%  $\text{Ag}_3\text{PO}_4$  in it possesses the optimal

photocatalytic RhB degradation performance. The photocatalytic degradation performance of the 64 wt%  $\text{Ag}_3\text{PO}_4/\text{Ag}/\text{WO}_{3-x}$  composite is increased by 4 times compared with that of  $\text{Ag}_3\text{PO}_4$ , and is increased by 3.7 times compared with that of the 64 wt%  $\text{Ag}_3\text{PO}_4/\text{WO}_3$  composite. The experimental results obtained in this work indicate that it has great potential significance to prepare the Z-scheme photocatalyst using the transition metal oxide.

#### Acknowledgements

This work was financially supported by the National Natural Science Foundation of China (Grant no. 41376126), the Hundreds-Talent Program of the Chinese Academy of Sciences (Y02616101L), Taishan Scholar and Qingdao Talents(13-CX-20).

#### Appendix A. Supplementary data

Supplementary data associated with this article can be found, in the online version, at <http://dx.doi.org/10.1016/j.apcatb.2015.05.045>.

#### References

- [1] M.R. Hoffmann, S.T. Martin, W. Choi, D.W. Bahnemann, Chem. Rev. 95 (1995) 69–96.
- [2] X. Chen, S. Shen, L. Guo, S.S. Mao, Chem. Rev. 110 (2010) 6503–6570.
- [3] H. Gerischer, Electrochim. Acta 38 (1993) 3–9.
- [4] X.C. Wang, K. Maeda, A. Thomas, K. Takanabe, G. Xin, J.M. Carlsson, K. Domen, M. Antonietti, Nat. Mater. 8 (2009) 76–80.
- [5] S.C. Yan, Z.S. Li, Z.G. Zou, Langmuir 25 (2009) 10397–10401.
- [6] Y. Bi, S. Ouyang, N. Umezawa, J. Cao, J. Ye, J. Am. Chem. Soc. 133 (2011) 6490–6492.
- [7] X. Yang, H. Cui, Y. Li, J. Qin, R. Zhang, H. Tang, ACS Catal. 3 (2013) 363–369.
- [8] W.K. H. Ng F. Wang, J.C. Yu, C. Zhu, L. Li, Z. Zhang, Q. Liu, Appl. Catal. B: Environ. 111–112 (2012) 409–414.
- [9] F. Wang, C. Li, Y. Li, J.C. Yu, Appl. Catal. B: Environ. 119–120 (2012) 267–272.
- [10] P. Wang, B. Huang, X. Qin, X. Zhang, Y. Dai, J. Wei, M.H. Whangbo, Angew. Chem. Int. Ed. 47 (2008) 7931–7933.
- [11] C. Hu, T. Peng, X. Hu, Y. Nie, X. Zhou, J. Qu, H. He, J. Am. Chem. Soc. 132 (2010) 857–862.
- [12] C. An, S. Peng, Y. Sun, Adv. Mater. 22 (2010) 2570–2574.
- [13] F. Lin, D. Wang, Z. Jiang, Y. Ma, J. Li, R. Li, C. Li, Energy Environ. Sci. 5 (2012) 6400–6406.
- [14] M. Liao, J. Feng, W. Luo, Z. Wang, J. Zhang, Z. Li, T. Yu, Z. Zou, Adv. Funct. Mater. 22 (2012) 3066–3074.
- [15] Y. Wang, Y.Y. Zhang, J. Tang, H. Wu, M. Xu, Z. Peng, X.G. Gong, G. Zheng, ACS Nano. 7 (2013) 9375–9383.
- [16] N. Feng, Q. Wang, A. Zheng, Z. Zhang, J. Fan, S.B. Liu, J.P. Amoureux, F. Deng, J. Am. Chem. Soc. 135 (2013) 1607–1616.
- [17] K. Li, B. Chai, T. Peng, J. Mao, L. Zan, ACS Catal. 3 (2013) 170–177.
- [18] H. Li, Y. Zhou, L. Chen, W. Luo, Q. Xu, X. Wang, M. Xiao, Z. Zou, Nanoscale 5 (2013) 11933–11939.
- [19] K. Maeda, ACS Catal. 3 (2013) 1486–1503.
- [20] A.J. Bard, J. Photochem. 10 (1979) 59–75.
- [21] H. Tada, T. Mitsui, T. Kiyonaga, T. Akita, K. Tanaka, Nat. Mater. 5 (2006) 782–786.
- [22] J. Li, S.K. Cushing, P. Zheng, T. Senty, F. Meng, A.D. Bristow, A. Manivannan, N. Wu, J. Am. Chem. Soc. 136 (2014) 8438–8449.
- [23] W. Z. Chen, Z. Wang, X. Fang Zhang, J. Phys. Chem. C 117 (2013) 19346–19352.
- [24] L. Ye, J. Liu, C. Gong, L. Tian, T. Peng, L. Zan, ACS Catal. 2 (2012) 1677–1683.
- [25] A. Iwase, Y.H. Ng, Y. Ishiguro, A. Kudo, R. Amal, J. Am. Chem. Soc. 133 (2011) 11054–11057.
- [26] X. Wang, G. Liu, L. Wang, Z.G. Chen, G.Q. Lu, H.M. Cheng, Adv. Energy Mater. 2 (2012) 42–46.
- [27] G. Xi, J. Ye, Q. Ma, N. Su, H. Bai, C. Wang, J. Am. Chem. Soc. 134 (2012) 6508–6511.
- [28] Z. Yi, J. Ye, N. Kikugawa, T. Kato, S. Ouyang, H. Stuart-Williams, H. Yang, J. Cao, W. Luo, Z. Li, Y. Liu, R. Withers, Nat. Mater. 9 (2010) 559–564.
- [29] M. Zhu, P. Chen, M. Liu, Chin. Sci. Bull. 58 (2013) 84–91.
- [30] Y.S. Sohn, Y.R. Smith, M. Misra, V. Subramanian, Appl. Catal. B: Environ. 84 (2008) 372–378.
- [31] X. Wang, L. Sø, R. Su, S. Wwindt, P. Hald, A. Mamakhe, C. Yang, B.B. Huang, F. Besenbacher, J. Catal. 310 (2014) 100–108.
- [32] R. Su, R. Tiruvalam, Q. He, N. Dimitratos, L. Kesavan, C. Hammond, J.A. Lopez-Sanchez, R. Bechstein, C.J. Kiely, G.J. Hutchings, F. Besenbacher, ACS Nano 6 (2012) 6284–6292.
- [33] T. Xu, L. Zhang, H. Cheng, Y. Zhu, Appl. Catal. B: Environ. 101 (2011) 382–387.
- [34] R. Chen, S. Zhao, X. Meng, H. Liu, Y. Wei, RSC Adv. 4 (2014) 47521–47528.
- [35] Y. Xu, M.A.A. Schoonen, Am. Mineral. 85 (2000) 543–556.